Journal of Sol-Gel Science and Technology (2019) 92:45–56
https://doi.org/10.1007/s10971-019-05073-5

ORIGINAL PAPER: FUNCTIONAL COATINGS, THIN FILMS AND MEMBRANES (INCLUDING DEPOSITION TECHNIQUES)

Check for updates

Electrochemical performance of $La_{0.6}Sr_{0.4}Co_{0.2}Fe_{0.8}O_3$–$Ce_{0.9}Gd_{0.1}O_{2-\delta}$ composite SOFC cathodes fabricated by electrocatalyst and/or electrocatalyst-ionic conductor infiltration

Can Sındıraç[1] · Aligül Büyükaksoy[2,3] · Sedat Akkurt[1]

Received: 28 March 2019 / Accepted: 2 July 2019 / Published online: 15 July 2019

Abstract

Infiltration of electrocatalyst precursor solutions into previously sintered porous ionic conductor scaffolds has been used recently as an alternative method to the conventional co-sintering route to fabricate electrocatalyst-ionic conductor composites for solid oxide fuel cell (SOFC) cathode applications. However, the aqueous nitrate solutions generally used to perform the infiltration process results in electrocatalyst precipitates that are disconnected from each other, yielding poor electrode performance. In this work, polymeric electrocatalyst ($La_{0.6}Sr_{0.4}Co_{0.2}Fe_{0.8}O_3$—LSCF) precursors that produce interconnected thin films upon heat treatment were used to infiltrate porous ionic conductor $Ce_{0.9}Gd_{0.1}O_{2-\delta}$ (GDC) scaffolds to overcome these issues. In addition, for the first time in the literature, a mixture of LSCF and GDC polymeric precursors, which would yield LSCF–GDC nanocomposite coatings on the grains of the porous GDC scaffold were used as the infiltration solution. Thus, further enhancement of the electrocatalyst/ionic conductor interfacial area and achievement of improved electrode performance was aimed. As a result of the optimization studies, the lowest measured area specific polarization resistance ($ASR_{cathode}$) values of 0.47 and 0.73 $\Omega.cm^2$ were obtained for polymeric LSCF+GDC and LSCF precursor infiltrations respectively at 700 °C, in air. In addition, LSCF+GDC infiltration yielded electrodes with much improved long-term stability in comparison to those obtained by LSCF infiltration.

Graphical Abstract

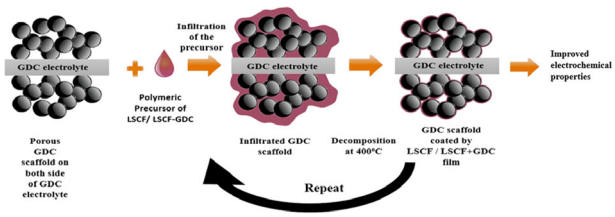

✉ Sedat Akkurt
sedatakkurt@iyte.edu.tr

[1] Department of Mechanical Engineering, Izmir Institute of Technology, Izmir, Turkey

[2] Department of Materials Science and Engineering, Gebze Technical University, Gebze, Turkey

[3] Gebze Technical University, Institute of Nanotechnology, Gebze, Turkey

Highlights

- Infiltration of LSCF and LSCF+GDC bearing solution into low-temperature fired GDC scaffold is successfully shown to improve the electrochemical performance of the SOFC cathode.
- Significant reductions in ASR values have been successfully achieved after infiltration.
- Long term stabilty was achieved when LSCF+GDC were infiltrated.

Keywords SOFC · GDC · LSCF · Impedance · Infiltration · Electrochemical performance

1 Introduction

Solid oxide fuel cells (SOFC) have attracted attention due to their potential for clean energy generation via the conversion of chemical energy directly into electrical energy without being restricted by Carnot efficiency [1, 2]. SOFCs allow the use of different fuels such as hydrocarbons, coal syngas and pure hydrogen [3]. Despite the significant progress that has been made, the cost and durability still remain a major barrier to the commercialization of SOFC technology [4]. High operating temperatures of traditional SOFCs (800–1000 °C) need to be lowered to reduce the cost of both materials and the electricity production [5, 6]. For example, if the SOFCs can be operated below 700 °C (intermediate temperatures), running costs may be reduced by allowing the use of cost-effective steel interconnects instead of expensive ceramic ones. The diffusion controlled chemical and microstructural degradation observed at high operating temperatures can also be prevented this way [7]. Moreover, lowering the operating temperatures can lead to shorter startup/shutdown time and enhanced SOFC system durability [8].

On the other hand, any reduction of the operation temperature has significant negative effects on SOFC performance due to lowered electrocatalytic activity of the electrodes [9] and increased ohmic losses [10]. As far as the electrolyte performance is concerned, the use of a thin electrolyte layer and/or an electrolyte with a higher ionic conductivity are proposed as alternatives to avoid performance loss in intermediate temperature (IT) SOFCs [11–14]. Improvements in the electrolyte layer are helpful but there is still room for further enhancement in performance of SOFCs for operation in the IT range. Studies have shown that as the operating temperature is reduced, cathode polarization resistance becomes the dominant factor limiting the SOFC performance [15–17]. Therefore, enhancement of the cathode performance for IT-SOFCs has been rigorously investigated [15–19]. Especially perovskite electrocatalysts that exhibit mixed ionic-electronic conductivity (MIEC) along with electrocatalytic activity for oxygen reduction, for example; $La_{1-x}Sr_xCo_{1-y}Fe_yO_3$ (LSCF), has shown promise, both as a single phase porous electrode and in the form of a perovskite-ionic conductor composite [16–20]. In the latter case, the main advantage of the ionic conductor addition has been to facilitate the oxygen ion transfer from the electrocatalyst to the ionic conductor by enhancing the interfacial area between these two phases [16, 20]. In addition to the choice of material, the process selected to fabricate the cathode layer is especially crucial to obtain low polarization resistances at the IT range, since it determines the microstructure of the cathode.

Conventional composite SOFC cathodes are prepared by co-firing of a mixture of powders of different particle sizes, surface areas and melting points which lead to different sintering temperatures and eventually uneven sintering. In addition, the relatively high sintering temperatures (1100–1300 °C) required to ensure bonding between (i) the cathode particles themselves, and (ii) the cathode-electrolyte interface yield large electrocatalyst particle sizes. This leads to diminished electrocatalyst-gas and electrocatalyst-ionic conductor interfacial areas and hence high cathode polarization resistances. Moreover, the formation of undesired phases with high resistivity, such $La_2Zr_2O_7$, has been reported under these processing conditions [21]. As an alternative strategy, infiltration (or wet impregnation) method has been proposed as an effective method to prepare electrocatalyst-ionic conductor composite cathodes [19, 20, 22]. In general, a liquid solution, typically composed of metal nitrates of the electrocatalyst cations dissolved in water, is introduced into a previously sintered porous ionic conductor scaffold layer formed on the electrolyte [23, 24]. Upon heating to 300–500 °C, salts are precipitated inside the pores and are subsequently calcined in order to form the desired oxide. This process is repeated several times to achieve the desired electrocatalyst loading within the pores of porous ionic conductor scaffold [23, 25]. The main advantage of the infiltration method is that it allows relatively low heat treatment temperatures (300–500 °C) which provide (i) large electrocatalyst/gas and electrocatalyst/ionic conductor interfacial areas, and (ii) minimized reactions between the infiltrated and scaffold phases and potentially high cathode performance [26].

Many researchers have studied the infiltration of aqueous solutions containing the nitrate salts of the cations constituting the MIEC perovskites [23–25]. It has been reported that LSCF infiltration into porous ionic conductor scaffold (e.g., GDC) results in improved performances over those fabricated by co-firing [20, 27, 28]. For example, an aqueous nitrate LSCF solution infiltration into porous GDC

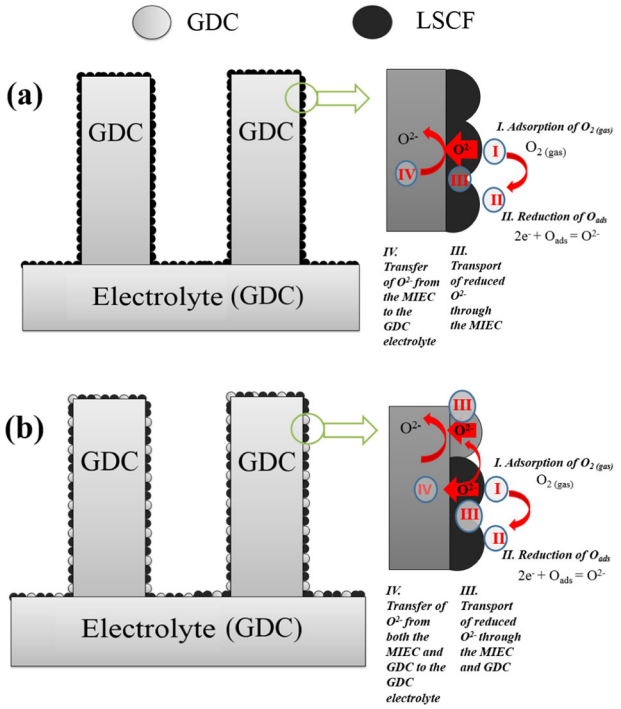

Fig. 1 Schematic representation of proposed pathways of oxygen ions at cathode layers prepared by **a** single phase LSCF and **b** LSCF+GDC polymeric precursor solution infiltration into porous GDC scaffolds

scaffolds was studied by Kim et al. who reported a polarization resistance of 1.7 Ω.cm^2 at 600 °C [29]. In the reverse case, Chen et al. indicated that infiltration of GDC into screen printed LSCF scaffold significantly reduced the polarization resistances down to 1.6 Ω.cm^2 from 5.4 Ω.cm^2 for pure LSCF cathode at 600 °C [30].

Despite these promising results reported in the literature, the potential of the infiltration approach cannot be fulfilled when aqueous nitrate solutions are used to infiltrate the porous scaffolds, as they yield segregated and disconnected particles, leading to the poor current collection and hence, insufficient performance. To address these issues, the use of polymeric precursors, which can form interconnected films upon decomposition, has been proposed as a more effective infiltration method [31, 32]. For example, $La_{0.8}Sr_{0.2}MnO_3$–$Zr_{0.84}Y_{0.16}O_2$ (LSM–YSZ) cathodes prepared by the infiltration of a polymeric LSM precursor into a porous YSZ scaffold has resulted in a polarization resistance as low as ca. 0.030 Ω.cm^2 at 800 °C [31]. This approach has also proven effective in the SOFC anode applications as polymeric Ni infiltration into porous YSZ scaffolds also exhibited very low polarization resistance of 0.1 Ω.cm^2 at the same temperature [33]. Obviously, the LSM–YSZ and Ni–YSZ systems are generic examples of composite SOFC electrode materials, both of which hosting the electrochemical reactions exactly at their electrocatalyst-ionic conductor-gas triple phase boundaries. Meanwhile, the formation of MIEC-ionic conductor composites using the polymeric precursor method has the potential to yield electrodes with electrochemical performances exceeding those of the above-mentioned generic composites prepared by the same method. Nonetheless, this direction has not been thoroughly explored to date, i.e., only one paper reporting polymeric LSCF precursor infiltration into porous GDC scaffolds exists [24].

In the present work, we propose to fabricate two types of LSCF–GDC composite cathodes by making use of the polymeric precursor method. The first type of composite is prepared by infiltrating a polymeric LSCF precursor into a porous GDC scaffold to obtain an interconnected LSCF film with high surface area over the scaffold particles. In this case, due to the MIEC nature of the LSCF film, the oxygen reduction reaction is considered to proceed in four steps, as depicted in Fig. 1a. These steps are: adsorption of oxygen to the LSCF surface (Step I), reduction of adsorbed oxygen into oxygen ion and its insertion into the LSCF lattice (Step II), the transport of the oxygen ion through the LSCF lattice to the LSCF/GDC interface (Step III) and the transfer of the oxygen ion from the LSCF to the GDC lattice (Step IV). Similar oxygen reduction schemes have been proposed in the literature for MIEC cathodes, such as LSCF [34]. The second type of LSCF–GDC composite is proposed to be fabricated by infiltrating a mixture of polymeric LSCF and GDC precursors again into a porous GDC scaffold, for the first time in the literature. We anticipate that, upon heating, the ions present in the polymeric precursor mixture will segregate preferentially to form the LSCF and GDC phases. In this case, as depicted schematically in Fig. 1b, an LSCF–GDC nanocomposite film will be formed on the grains of the porous GDC scaffold. A performance enhancement with respect to single phase GDC infiltration is expected due to the enhancement of the LSCF/GDC interfacial area and the consequent facilitation of oxygen ion transfer between the MIEC and the ionic conductor phases (Step IV). For both types of infiltration, the number of infiltration cycles were optimized to achieve the lowest polarization resistance possible at 700 °C.

2 Experimental

2.1 Fabrication of the dense GDC electrolytes and porous GDC scaffolds

10 mol% gadolinium-doped ceria powders ($Ce_{0.9}Gd_{0.1}O_{2-d}$, Praxair, >99.9%, with 6.5 m^2/g specific surface area were used in the manufacture of the dense ceramic electrolyte by uniaxial pressing (Carver Hydraulic Press, Wabash, IN, USA) at 180 MPa in a cylindrical stainless steel die with 15 mm diameter and ~1.5 mm height. The pellets were fired at 1400 °C for 4 h at a heating rate of 3 °C/min in a laboratory kiln (Nabertherm LHT02/17, Germany).

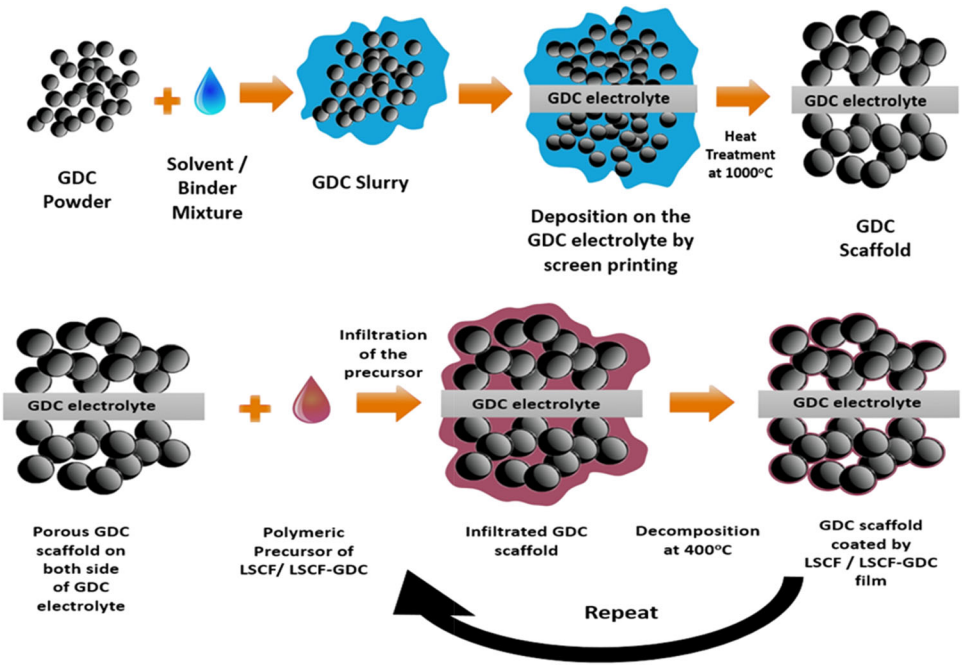

Fig. 2 Schematic representation of experimental flow chart depicting the formation of the porous scaffold, and the infiltration of the scaffold multiple times to deposit nano-sized LSCF or LSCF+GDC

2.2 Preparation of polymeric precursors and the infiltration process

Precursor solution of LSCF was prepared by dissolving proper amounts of lanthanum (III) nitrate hexahydrate (ALFA-AESAR >99.99%), strontium chloride hexahydrate (ALFA-AESAR >99%), cobalt (II) nitrate hexahydrate (ALFA-AESAR >97.7% min), iron (III) nitrate nonahydrate (ALFA-AESAR >99.99%) salts in deionized water at a molar ratio that would yield the of LSCF 6428 stoichiometry. The solutions were then mixed with ethylene glycol, ensuring that the molar ratio of the total metal salts to ethylene glycol was 0.02. Upon stirring at 70 °C, all water evaporated, leaving a non-aqueous and more viscous solution which was then diluted by the addition of 2-butoxyethanol solution in 1:1 weight ratio, aiming to enhance the wetting properties of the precursor. A polymeric GDC precursor was also prepared from cerium nitrate hexahydrate (ALFA-AESAR >99.5%) and gadolinium nitrate hexahydrate (Sigma-Aldrich >99.9%) salts following the same procedures. For LSCF+GDC infiltration, the polymeric LSCF and GDC precursor solutions were mixed in appropriate amounts that would yield a 60:40 volumetric LSCF to GDC ratio upon heat treatment.

Figure 2 summarizes the infiltration process. To form the porous GDC scaffold layer on the dense GDC electrolyte, a slurry consisting of GDC powder dispersed in α-terpineol and 2-butoxyethanol was prepared. The slurry was deposited on both sides of the dense GDC electrolyte by brush-painting before being partially sintered at 1000 °C for 2 h. The polymeric precursor solution of LSCF/LSCF+GDC was infiltrated into the previously formed porous GDC scaffold layers by brushing on both sides of the electrolyte. Heat treatment at 400 °C on hot plate drove off volatiles thus completing one infiltration cycle. Different number of infiltration cycles (10–50) were carried out in this study to determine optimum loadings. Samples were encoded according to the infiltration precursor type and number of infiltration cycles. For example, LSCF 40X denotes 40 cycles of LSCF infiltration, while LSCF+GDC 30X represents 30 cycles of infiltration using a mixture of polymeric LSCF and GDC precursors.

2.3 Crystal structure and microstructure analyses

Crystal structures of the composite cathodes were determined by X-ray diffraction (XRD- Panalytical X'Pert Pro, CuKα radiation). However, the interpretation of the composite cathodes, especially those prepared by LSCF +GDC infiltration into porous GDC scaffold is quite difficult, as it cannot be decided with acceptable certainty whether any cubic GDC peaks that are likely to appear, originate from the substrate, the porous scaffold or from the infiltrated polymeric precursor. To avoid such complications, the XRD analyses were performed on dried gels of LSCF and LSCF+GDC polymeric precursors calcined at 700 °C.

The microstructures and morphologies of the LSCF and LSCF+GDC infiltrated and non-infiltrated porous GDC scaffolds were examined by scanning electron microscope (SEM, Philips XL 30S FEG) using secondary electron imaging and the elemental compositions of the cathode layers were determined by energy dispersive X-ray spectroscopy (EDX) analysis.

2.4 Electrochemical performance analysis

For the evaluation of the electrochemical performance of the fabricated cathodes, an in-house Ag paste was brush-painted onto the cathode surfaces in order to form current collecting layers which were connected to Ag lead wires. Autolab (Metrohm M204 PGSTAT) instrument was used to analyze the electrochemical performance of the symmetrical half-cells by electrochemical impedance spectroscopy (EIS) at 500–700 °C, in stagnant air with an AC amplitude of 15 mV excitation voltage amplitude. Nova 2.1 software was used to fit the collected EIS data.

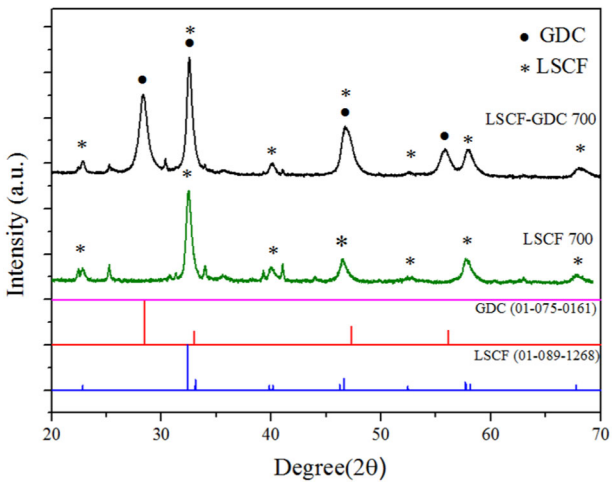

Fig. 3 X-ray diffraction (XRD) patterns obtained from gels obtained by drying LSCF and LSCF+GDC precursor solutions and further heat treated at 700 °C

3 Results and discussion

To determine the phases in which the infiltration solutions form within the porous GDC scaffold, the dried gels of the LSCF and LSCF+GDC polymeric precursors were calcined at 700 °C and were subjected to X-ray diffraction (XRD) analyses. XRD patterns of these powders show the presence of rhombohedral LSCF phase (PDF: 01-089-1268) in both cases (Fig. 3). LSCF+GDC powder, also contains cubic GDC phase (PDF: 01-075-0161), as expected (Fig. 3). Unidentified peaks with low intensities at $2\theta = 25.3$, 35, 39, and 44° are also observed, indicating the presence of small amounts of impurity phases (Fig. 3). In the literature, LSCF and LSCF–GDC thin films prepared by spray pyrolysis were also reported to have similar unidentified peaks [35–41]. For example, unidentified peaks were observed at $2\theta = 35^{o}$ by Haider et al. [41], at $2\theta = 25.5$ and 44^{o} by Muller et al. [35]. These peaks were, however, found to disappear upon thermal treatment above 700 °C. Darbandi et al. [39] reported extra peaks at $2\theta = 25.5$, 36, 44^{o} which are traces of $SrNO_3$ which is commonly observed by other groups during LSCF formation [40].

As mentioned before, two different polymeric precursor solutions were used to infiltrate the porous GDC scaffold. Different numbers of infiltration cycles have been performed to ensure continuous coverage of the GDC particle surfaces of the porous scaffold with interconnected films of LSCF and LSCF+GDC, as opposed to discrete particles. Figure 4a depicts a representative cross-sectional scanning electron microscopy (SEM) image of a selected infiltrated sample (LSCF×40), revealing the GDC electrolyte, porous

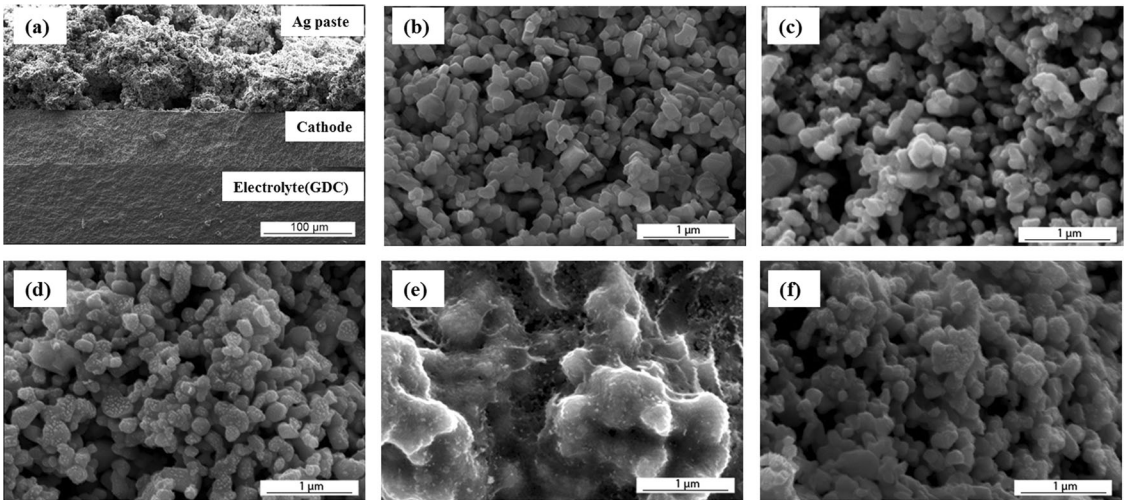

Fig. 4 Scanning electron microscopy (SEM) images of fractured cross sections of **a** a representative LSCF+GDC infiltrated cathode (40x) also including the Ag current collector and the electrolyte, **b** a previously sintered porous GDC scaffold layer without any infiltration, **c** porous GDC scaffold infiltrated 45 times with LSCF precursor solution after annealing at 700 °C for 2 h **d** porous GDC scaffold infiltrated 30 times with LSCF+GDC solution after annealing at 700 °C for 2 h, porous GDC scaffold infiltrated 45 times by LSCF precursor solution and heat treated at 700 °C for 100 h, **f** porous GDC scaffold infiltrated 30 times by LSCF+GDC precursor solution and heat treated at 700 °C for 100 h

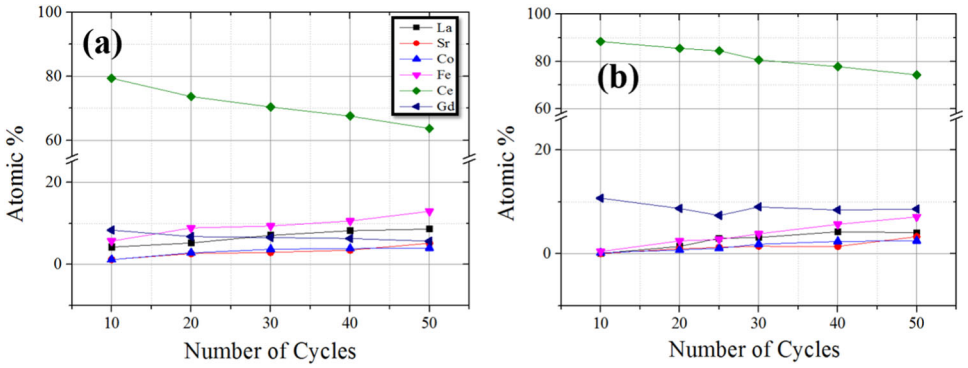

Fig. 5 Relative amounts of La, Sr, Co, Fe, Ce, and Gd elements determined by energy dispersive X-ray spectroscopy (EDX) measurements performed at the middle part of the cathode layers prepared by **a** LSCF and **b** LSCF+GDC infiltration into porous GDC scaffolds

GDC scaffold, and Ag current collector layers. A good adherence between the porous GDC scaffold and the dense GDC electrolyte can be clearly observed with an approximate thickness of 65–75 µm. The SEM image of the non-infiltrated porous GDC scaffold layer is shown in Fig. 4b. Evidently, the porous GDC layer consists of grains and pores with uniformly distributed sizes, originating from partial sintering of the as-received GDC powder.

The microstructural characterization of the infiltrated composite cathodes were also performed in more detail before and after long-term (i.e., 100 h) testing at 700 °C to (i) ensure that interconnected films are formed on the grains of the porous GDC scaffold, not discrete particles and (ii) observe any significant microstructural changes that may take place upon prolonged exposure to the operating temperature (700 °C). Both the LSCF and the LSCF+GDC infiltrated cathodes resemble the blank GDC scaffold microstructure and appear to contain only a few discrete particles (Fig. 4c, d), i.e., much less than the infiltrated amount. This suggests that the polymeric precursor infiltration results in interconnected film formation on the scaffold grains (Fig. 4c, d). After long-term stability test, microstructures do not appear to be significantly changed in LSCF (Fig. 4e) and LSCF+GDC (Fig. 4f) samples i.e. grain size, porosity and agglomeration.

Energy dispersive X-ray spectroscopy (EDX) analyses over the fractured cross section of samples were performed to track the variation of elemental concentration within the cathode layer after different infiltration cycles (Fig. 5). As stated above, the infiltration solutions were prepared to yield the exact stoichiometries of $La_{0.6}Sr_{0.4}Co_{0.2}Fe_{0.8}O_{3-\delta}$ and $Ce_{0.9}Gd_{0.1}O_{2-\delta}$. Figure 5a shows the elemental percentage change of LSCF infiltrated cathode with an increasing number of infiltration cycles. The relative amounts of Ce and Gd decreases while those of La, Sr, Co, and Fe increases with increasing number of infiltration cycles, which is expected (Fig. 5a) Increasing the number of infiltration cycles cause a fast increase in the Fe content, and a slower increase in the relative amounts of other elements (i.e., La, Sr, Co), as dictated by the LSCF stoichiometry. In

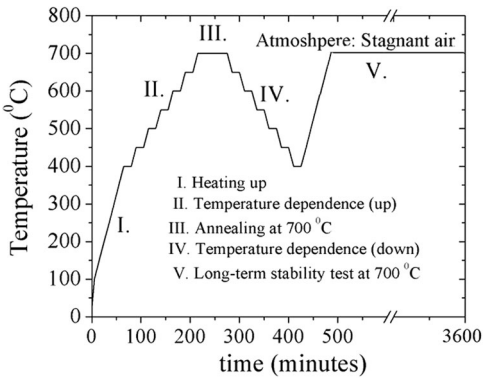

Fig. 6 Heating/cooling schedule followed during impedance spectroscopy measurements

the case of LSCF+GDC infiltration (Fig. 5b), increasing the number of infiltration cycles leads to an enrichment of the electrocatalyst elements as expected, but this time to a lesser extent due to the GDC content of infiltrating solution.

The electrochemical performance of the infiltrated electrodes were determined by electrochemical impedance spectroscopy (EIS) measurements of the symmetrical half-cells at 500–700 °C, in stagnant air. Since the thermal history of the infiltrated electrodes may have a significant impact on the electrochemical performance, the heat treatments that the infiltrated cathodes had been subjected to at the time of measurement are described in detail in Fig. 6. Here, the heating regime consists of five stages and the EIS measurements are collected at every 50 °C when cooling down from 700 °C (Stage IV) and intermittently upon long-term exposure to 700 °C (Stage V).

Nyquist and Bode plots of the EIS data collected at 700 °C from the cathodes prepared by 10–50 cycles of polymeric precursor infiltration are shown in Fig. 7. The equivalent circuit models used to fit the EIS data are also provided as insets in the Nyquist plots (Fig. 7). Curve fits using the related equivalent circuits were achieved with negligible error ($\chi^2 \sim 10^{-4}$). The series resistances present in the equivalent circuits are denoted as "Rs" and are obtained from the intercept of the impedance response at

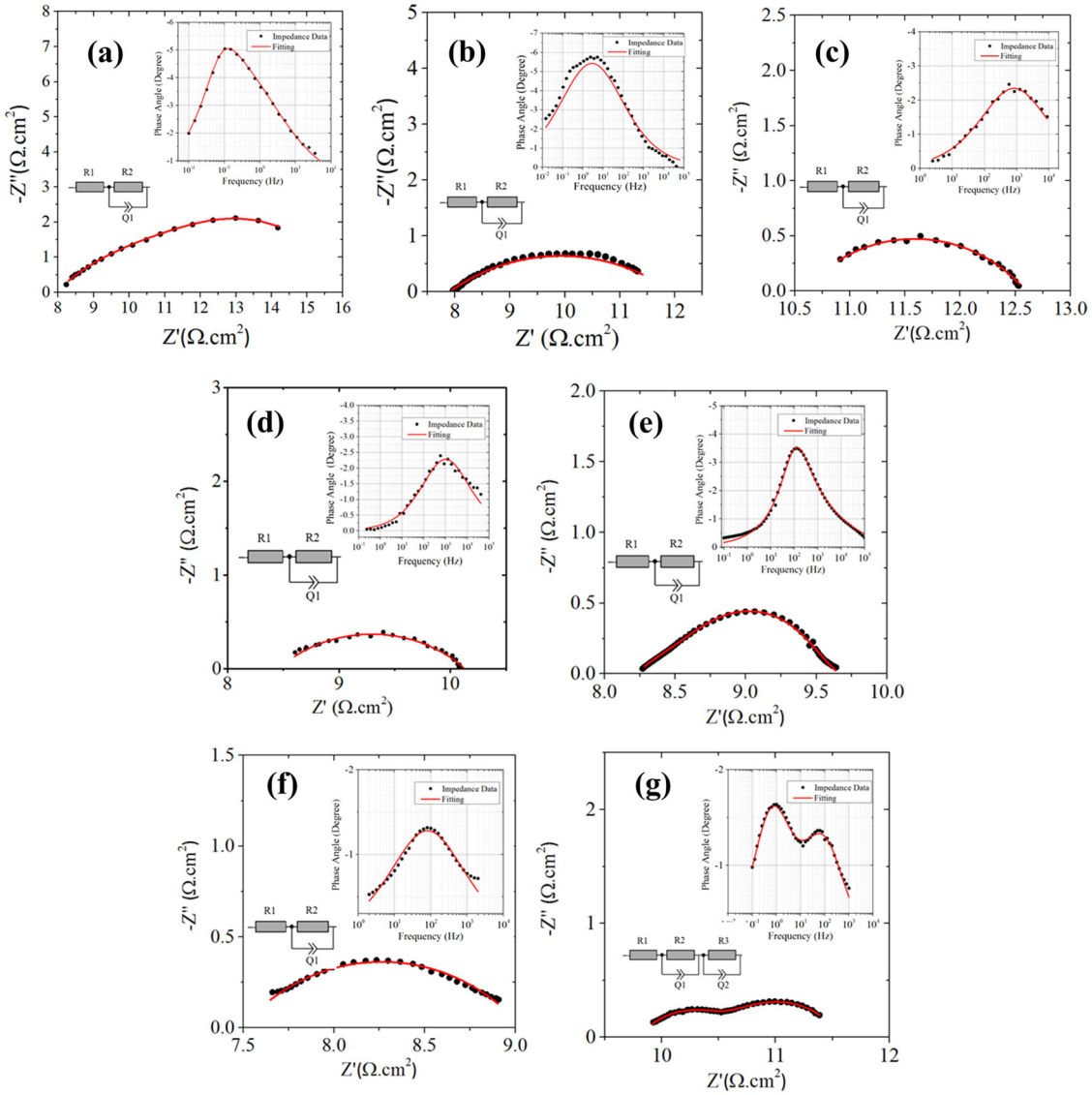

Fig. 7 Impedance spectra obtained from cathodes prepared by **a** 10× **b** 20× **c** 30× **d** 35x **e** 40× **f** 45× **g** 50× LSCF infiltration into porous GDC scaffolds. Measurements were conducted on symmetrical half cells at 700 °C, in air. The equivalent circuit models used to fit the obtained impedance data are provided in insets

high frequency. This contribution is related to the electrolyte resistance and is slightly variable from sample to sample due to the variations in the thickness of the electrolyte substrate. The size of the impedance arc (R1 or the sum of R1 and R2 in one case) refers to the polarization resistances of the two identical electrodes. Hence, the polarization resistance value should be divided by two to find the area specific polarization resistance per each infiltrated cathode ($ASR_{cathode}$).

Measured impedance data for samples infiltrated 10–45 times show a similar type of EIS response, i.e., a single semi-circle which corresponds to an equivalent circuit consisting of electrolyte resistance (Rs) coupled in series with a polarization resistance connected in parallel to a constant phase element unit (R1/Q1) (Fig. 7a–f). Evidently, the general tendency is that an increase in the number of LSCF infiltration cycles brings about reductions in the polarization resistance (Fig. 7a–f). For example, the polarization resistance per electrode decreases from 9.04 Ω.cm^2 down to 0.71 Ω.cm^2 at 700 °C upon an increase in the number of LSCF infiltration cycles from 0 to 40 (Fig. 7a–f). This is expected since the increased number of LSCF infiltration cycles enhances the coverage of the GDC grain surfaces of the porous scaffold with the electrocatalytic LSCF film providing more LSCF/gas and LSCF/GDC interfacial area. On the other hand, no further reductions in the polarization resistance is observed when the number of infiltration cycles is increased from 40 to 45 (Fig. 7e–g). Furthermore, an increase in the polarization resistance up to 1.57 Ω.cm^2 concomitant with the appearance of a low-

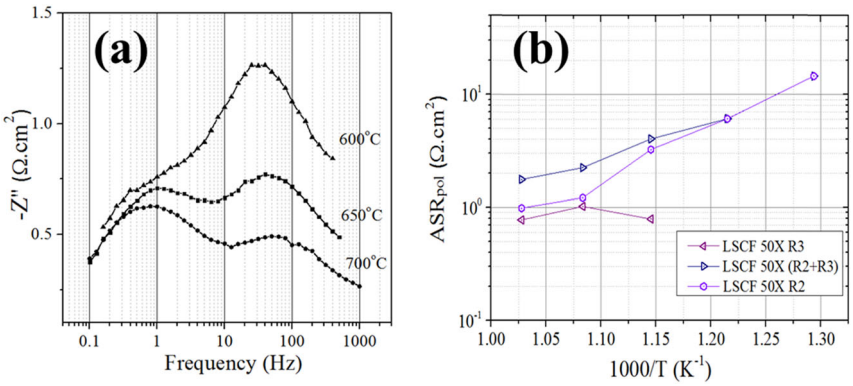

Fig. 8 **a** Bode plots showing the impedance response of LSCF (50×) infiltrated symmetrical half-cell measured at 600, 650, and 700 °C. **b** Temperature dependence of the cathode polarization resistance of infiltrated LSCF (50×) sample, also showing the individual contributions of the high and low-frequency resistance components (i.e., R2 and R3) to total resistance. Impedance spectroscopy measurements were performed on symmetrical half-cells cells, in air

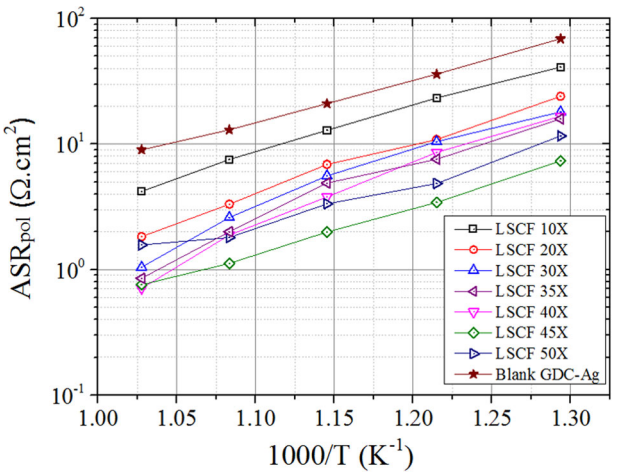

Fig. 9 Temperature dependence of the cathode polarization resistances obtained from the impedance spectroscopy measurements of symmetrical half-cells with cathode layers prepared by different amounts of (from 10x to 50x) LSCF infiltration. Cathode polarization resistance of blank porous GDC layer brushed with silver current collector was also added for comparison

Table 1 Cathode polarization resistance values (per electrode) and the corresponding activation energies of LSCF infiltrated cathodes for prepared by different number of infiltration cycles measured at 700 °C

Sample Name	Ea (eV)	Rp at 700 °C (per electrode) (Ω.cm²)
Blank GDC -Ag Collector	0.74	9.04
LSCF 10×	0.81	4.2
LSCF 20×	0.89	1.83
LSCF 30×	0.99	1.04
LSCF 35×	1.00	0.85
LSCF 40×	1.08	0.71
LSCF 45×	0.95	0.73
LSCF 50×	0.73	1.57

frequency semi-circle represented with another resistor/constant phase element in the equivalent circuit diagram (R2/Q2) in the 50× LSCF electrode is evident (Fig. 7g). In the literature the low-frequency semi-circle has been attributed either to concentration polarization resulting from the insufficient porosity [42, 43], or to the chemical capacitance originating from the oxygen insertion into the MIEC lattice and the consequent changes in the oxidation states of the transition metal cations within the perovskite structure [42–47]. Considering the temperature dependence of these processes, the EIS measurements of the symmetrical cell with 50× LSCF electrodes have been carried out at different temperatures to determine the physical cause of the low-frequency arc observed in these cathodes. The EIS data obtained at 600, 650, and 700 °C are represented in the form of a Bode plot in Fig. 8a to clearly show the effect of temperature on the high and low-frequency processes. Here, the imaginary part of the impedance remains unchanged at low-frequency range (at around 0.4 Hz) but is found to increase with decreasing temperature at high frequencies (at around 30 Hz, Fig. 8a). The temperature dependence of the area specific resistances of the high and low-frequency processes (denotes as R1 and R2, respectively), their sum (total polarization resistance) determined from the equivalent circuit fitting of the EIS response of LSCF 50× (R1 + R2) are given in Fig. 8b. Evidently, R1 obtained from LSCF 50× has a strong dependence on temperature, while R2 remains nearly unchanged (Fig. 8b). The temperature independent nature of R2 suggests that the low-frequency process is concentration polarization, likely caused by the overloading of the porous GDC scaffold with infiltrated LSCF, thereby eliminating porosity required for the transport of oxygen gas to the electrochemically active surfaces.

In order to examine the performance of the LSCF infiltrated cathodes at intermediate temperatures (500–700 °C), EIS measurements were performed in the range of

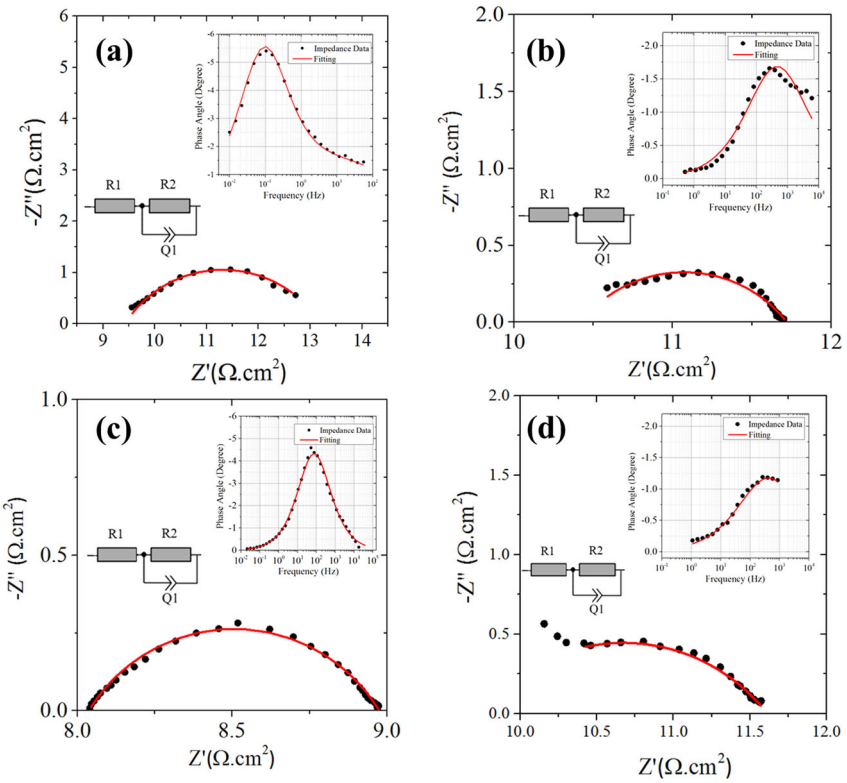

Fig. 10 Impedance spectra obtained from cathodes prepared by **a** 10× **b** 20× **c** 30× **d** 40× LSCF+GDC infiltration into porous GDC scaffolds. Measurements were conducted on symmetrical half cells at 700 °C in air. The equivalent circuit models used to fit the obtained impedance data are provided in insets

500–700 °C temperature range. Temperature dependences of the total area specific polarization resistance (ASR) values of infiltrated LSCF+GDC cathodes are plotted as $ASR_{cathode}$ vs 1000/T (Fig. 9). The data collected from the symmetrical half-cells with blank porous scaffold layers with only Ag current collectors is also included to serve as a reference (Fig. 9). $ASR_{cathode}$ consistently increases with decreasing measurement temperature (700 down to 500 °C) and decreases with increasing the number of LSCF infiltration cycles. Similar slopes referring to similar activation energies in the range of 0.81–1.08 eV are visible for all samples, except for LSCF 50x, which exhibits a weaker temperature dependence due to the presence of the temperature independent low-frequency process attributed to concentration polarization herein (Table 1).

Su et al. [48] defined a promotion factor for infiltrated electrodes as $\varepsilon = Rp_{blank}/Rp_{inf}$ where Rp_{blank} is the polarization resistance of the non-infiltrated cathode and Rp_{inf} is the polarization resistance of infiltrated cathode to examine the success of infiltration. Tomov et al. [43] systematically grouped different studies [49–51] based on their promotion factor (ε) which varies from 1.30 to 3.66 for GDC infiltration into LSCF scaffold of different loadings. The ε values measured in this study varies between 1.99 and 12.3 for the LSCF infiltrated cathodes, suggesting that the polymeric precursor method is very effective for infiltration purposes.

Evolution of the EIS response of the polymeric LSCF +GDC precursor infiltrated composite cathodes with varying number of infiltration cycles is shown in Fig. 10. Only one depressed semi-circle is observed in the Nyquist plots of all samples. Thus, the proposed equivalent circuit used for fitting the curve has two resistance components Rs (electrolyte resistance) and R1 (polarization resistance). In the circuit, Rs represents the ohmic resistance of the GDC electrolyte and R1/Q1 elements represent electrode processes. Resembling the case of LSCF infiltration, increasing the number of LSCF+GDC infiltration cycles from 10× to 30× brings about a significant reduction in the polarization resistance values, while further increasing the number of infiltration cycles has negative effect on the electrochemical performance at 700 °C. Polarization resistances as low as ~0.47 Ω.cm² per electrode at 700 °C are obtained in the case of 30× LSCF+GDC infiltration (Fig. 10c). The ε values varying between 3.72 and 19.23 obtained in the case of LSCF+GDC infiltrated samples reflect the superiority of these cathodes over those prepared by LSCF infiltration. The reason for the lower value of the lowest possible polarization resistance value obtained in the case of LSCF +GDC infiltration in comparison to that obtained by LSCF infiltration is the enhancement of the electrocatalyst/ionic conductor interfacial area and thus facilitated oxygen ion transfer to the electrolyte, as proposed in Fig. 1b. The increase in the polarization resistance observed upon

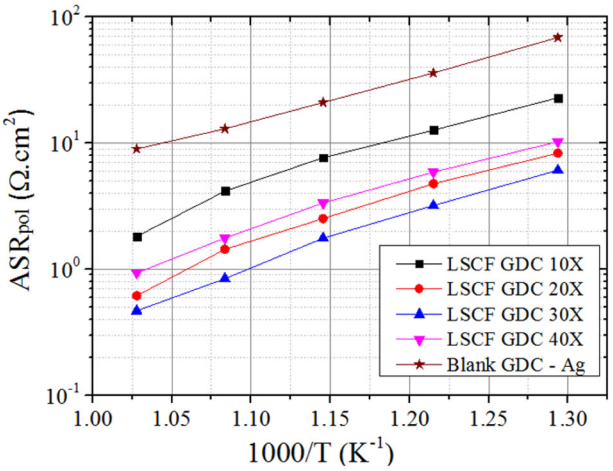

Fig. 11 Temperature dependence of the cathode polarization resistances obtained from the impedance spectroscopy measurements of symmetrical half-cell with cathodes prepared by different amounts of (from 10x to 40x) LSCF+GDC infiltration into porous GDC scaffolds. Cathode polarization resistance of blank porous GDC layer brushed with silver current collector was also added for comparison

exceeding the optimum number of infiltration cycles (evidently 30X in this case) is not accompanied by the appearance of a concentration polarization related low-frequency semi-circle (Fig. 10d). A possible explanation lies in the formation of a very thick LSCF–GDC coating on the GDC grains, which increases the oxygen ion transport distances, leading to increased resistances. After excessive loading via infiltration similar performance losses were also observed in other studies which attributed the losses to the formation of clusters and thick coating that reduced the number of active sites [52, 53].

The variation of the area specific resistances (ASR) of LSCF+GDC infiltrated cathode samples with temperature for different number of infiltration cycles are shown in Fig. 11. Ag current collector data are included for comparison. These results revealed that increasing the LSCF+GDC infiltration cycles from 10× to 30×, the electrochemical performances of cathodes was enhanced regardless of measurement temperature. Similar activation energies in the range of 0.86–0.91 eV are visible for all samples (Table 2).

The long-term stability of the electrochemical performances of SOFC cathodes prepared by LSCF and LSCF + GDC infiltration into porous GDC scaffolds is tested by intermittently performing EIS measurements upon long-term exposure to 700 °C, which corresponds to the Stage V in Fig. 6. As shown in Fig. 12, a significant increase in the $ASR_{cathode}$ (from 0.73 Ω.cm^2 to 2.3 Ω.cm^2) takes place with time for single phase LSCF infiltrated cathode. The preliminary 60 hours of tests indicate a significantly improved longevity in the case of LSCF+GDC infiltrated cathodes (Fig. 12). In the literature, it has been reported that the addition of a secondary phase has been reported to inhibit

Table 2 Cathode polarization resistance values (per electrode) and the corresponding activation energies of LSCF infiltrated cathodes for prepared by different number of infiltration cycles measured at 700 °C

Sample Name	Ea (eV)	Rp at 700 °C (per electrode) (Ω.cm^2)
Blank GDC -Ag Collector	0.74	9.04
LSCF GDC 10x	0.86	1.82
LSCF GDC 20x	0.90	0.61
LSCF GDC 30x	0.91	0.47
LSCF GDC 40x	0.88	0.93

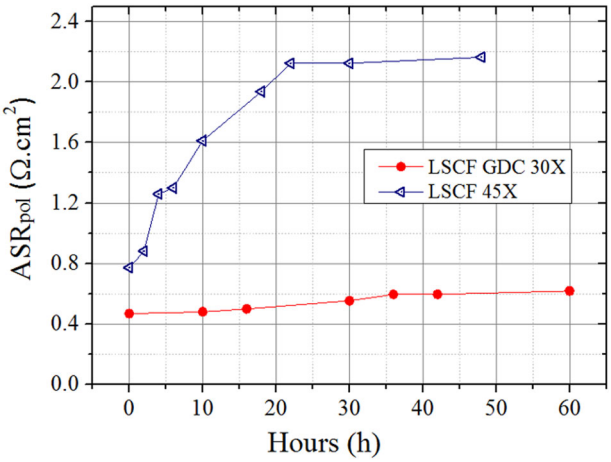

Fig. 12 Long-term stability test results (polarization resistance measured at 700 °C) of the symmetrical cells with LSCF 45× and LSCF +GDC 30× infiltrated as a function of dwell time

the grain growth and hence the loss of the MIEC/gas interfacial area in the case of conventionally prepared samples [54, 55]. The addition of GDC to the LSCF coatings formed on the grains of the porous GDC scaffolds is considered to induce such a microstructural stabilization in the present case as well. More detailed microstructural analyses via transmission electron microscopy required to test this hypothesis are currently underway.

4 Conclusion

Dense GDC electrolyte pellets fired to sufficiently high density were coated by screen printing to form a porous GDC layer on both sides to provide a porous GDC scaffold into which polymeric precursor solutions of LSCF and LSCF+GDC were successfully infiltrated by a multistep process. SEM analysis showed that, after infiltration, no agglomerates formed in any of the samples, suggesting that polymeric LSCF and LSCF+GDC precursors could coat the GDC particles in a uniform and effective manner. EIS measurements of the samples between 500 and 700 °C

clearly showed that increasing the amount of infiltration cycles enhanced the electrochemical performance up until 45x for LSCF and 30x for LSCF+GDC infiltration. Any further LSCF infiltration cycle only degraded the ASR manifesting itself by a low-frequency arc in the Nyquist diagrams, interpreted as a result of slowed mass transport of oxygen gas within the porous electrode. Loss of electrochemical performance after excessive LSCF+GDC infiltration was attributed to the formation of relatively thicker LSCF+GDC coatings on the grains of the porous GDC scaffold that brings about longer pathway for reduced oxygen ion transport from cathode to electrolyte. Comparison of the long-term electrochemical testing of the LSCF and LSCF+GDC infiltrated cathodes revealed that LSCF +GDC infiltration resulted in i) a higher electrochemical performance, attributed to enhanced LSCF/GDC interfacial area and ii) a more stable polarization resistance at 700 °C, likely originating from the inhibition of the grain growth in the LSCF phase by the GDC particles formed within the infiltrated coating. These results proved that precursor infiltration method is a very promising approach for the fabrication of high-performance cathodes for SOFC applications in intermediate temperatures.

Acknowledgements Authors would like to thank different labs in both Izmir Institute of Technology and Gebze Technical University for their helps during analysis of samples. This project is supported by Izmir Institute of Technology (BAP project numbers: 2016IYTE01 and 2017IYTE08).

Compliance with ethical standards

Conflict of interest The authors declare that they have no conflict of interest.

References

1. Kalinci Y, Dincer I (2018) Int J Hydrog Energy 43 (11):5795–5807
2. Sindirac C, Akkurt S (2016) Int J Hydrog Energy 41 (40):18157–18165
3. Yildiz B, Kazimi MS (2006) Int J Hydrog Energy 31(1):77–92
4. Perry ML, Fulller TF (2002) J Electrochem Soc 149(7):569–567
5. Nie L, Liu Z, Liu M,Yang L, Zhang Y, Liu M (2010) J Electrochem Sci and Tech 1(1): 50–56
6. Buyukaksoy A, Birss VI (2015) ECS Trans 66(2):267–274
7. Chunhua C, Bouwmeester JMH, Kruidhof H, ten Elshof JE, Burggraaf AJ (1996) J Mat Chem 6:815–819
8. Bohac P, Gauckler LJ (1999) Solid State Ionics 119(1–4):317–321
9. Sun C, Hui R, Roller J (2010) J Solid State Electrochem 14:1125
10. Steele BCH (2000) Solid State Ion 129:95
11. Li ZP, Toshiyuki M, Auchterlonie GJ, Zou J, John D (2011) ACS Appl Mater Interfaces 3(7):2772–2778
12. Steele BCH, Heinzel A (2001) Nature 414:345
13. Buyukaksoy A, Birss VI (2016) J Power Sources 307:449–453
14. Wang WG, Mogensen M (2005) Solid State Ion 176:457–462
15. Steele BCH (1995) Solid State Ion 75:157
16. Gauckler LJ, Beckel D, Buergler B, Jud E, Muecke UP, Prestat M, Rupp J, Richter J (2004) Chimia 58:837
17. Murray EP, Sever MJ, Barnett SA (2002) Solid State Ion 148:27
18. Barfod R, Hagen A, Ramousse S, Hendirksen PV, Mogensen M (2006) Fuel Cells 6:141
19. He HP, Huang YY, Regal J, Boaro M, Vohs JM, Gorte RJ (2004) J Am Ceram Soc 87:331
20. Shah M, Barnett SA (2008) Solid State Ion 179:2059–2064
21. Jiang SP (2008) J Mater Sci 43:6799
22. Murray EP, Barnett SA (2001) Solid State Ion 143:265–273
23. Gorte RJ, Park S, Vohs JM, Wang CH (2000) Adv Mater 12 (148):1465–1469
24. Chrzan A, Karczewski J, Gazda M, Szymczewska D, Jasinski P (2017) J European. Ceram Soc 37(11):3559–3564
25. Jiang SP (2012) Int J Hydrog En 37:449–470
26. Samsonz A, Søgaard M, Knibbe R, Bonanos N (2011) J Electrochem Soc 158:650–659
27. Liu Y, Wang F, Chi B, Pu J, Jian L, Jiang SP (2013) J Alloy Compd 578:37–43
28. Shah M, Voorhees PW, Barnett SA (2011) Solid State Ion 187 (1):64–67
29. Kim JH, Kim H (2012) Ceram Int 38(6):4669–4675
30. Chen J, Liang FL, Chi B, Pu J, Jiang SP, Li J (2009) J Power Sources 194:275–280
31. Buyukaksoy A, Petrovsky V, Dogan F (2012) J Electrochem Soc 159(1):B67–B71
32. Lou XY, Liu Z, Wang SZ, Xiu YH, Wong CP, Liu ML (2010) J Power Sources 195:419–424
33. Buyukaksoy A, Kammampata SP, Birss VI (2015) J Power Sources 287:349–358
34. Wang Z, Peng R, Zhang W, Wu X, Xia C, Lu Y (2013) J Mater Chem A 1:12932–12940
35. Muller G, Ringuede A, Laberty-Robert C (2014) J Mater Chem A 2:6448
36. Xi X, Kondo A, Kozawa T, Naito M (2016) Adv Powder Techn 27:646–651
37. Ghosh S, Dasgupta S (2010) Mater Sci-Poland 28(2):427–438
38. Leng Y, Chan SH, Liu Q (2008) Int J Hydrog Ener 33:3808–3817
39. Darbandi AJ, Hahn H (2009) Solid State Ion 180(26-27):1379–1389
40. Beckel D, Dubach A, Grundy AN, Infortuna A, Gauckler LJ (2008) J Ceram Soc 28:49
41. Haider MA, McIntosh S (2011) J Electrochem Soc 158(9): B1128–B1136
42. Molero-Sanchez B, Addo P, Buyukaksoy A, Paulson S, Birss V (2015) Faraday Discuss 182:159
43. Tomov RI, Mitchell-Williams T, Gao C, Kumar RV, Glowacki BA (2017) J Appl Electrochem 47:641–651
44. Dusastre V, Kilner JA (1999) Solid State Ion 126(1-2):163
45. Molero-Sanchez B, Addo P, Buyukaksoy A, Birss V (2017) J Electrochem Soc 164(10):F3123–F3130
46. Wei B, Liu Z, Wei T, Jia D, Huang X, Miao J, Su W (2011) Int J Hydrog En 36:6151–6159
47. Liu J, Co AC, Paulson SC, Birss VI (2006) Solid State Ion 177:377–387
48. Su F, Zhang Y, Ni M, Xia CH (2014) Int Hydrog En 39:2685–2691
49. Chen J, Liang F, Chi B, Pu J, Jiang SP, Jian L (2009) J Power Sources 194:275–280
50. Nie LF, Liu MF, Zhang YJ, Liu ML (2010) J Power Sources 19:4704–4708
51. Zhao E, Jia ZH, Zhao L, Xiong Y, Sun C, Brito ME (2012) J Power Sources 219:133–139

52. Liu M, Ding D, Blinn K, Xi X, Nie L, Liu M (2012) Int J Hydrog Energy 37:8613–8620
53. Barbucci A, Carpanese M, Reverberi AP, Cerisola G, Blanes M, Cabot PL, Viviani M, Bertei A, Nicolella C (2008) J Appl Electrochem 38:939–945
54. Chen J, Liang F, Yan C, Pu J, Chi B, Jiang SP, Jian L (2010) J Power Sources 195:5201
55. Fu C, Sun K, Zhang N, Chen X, Zhou D (2007) Electrochim Acta 52:4589–4594